NRC·CNRC

NRC Publications Archive
Archives des publications du CNRC

Experimental emulator of pulse dynamics in fractional nonlinear Schrödinger equation

Liu, Shilong; Zhang, Yingwen; Virally, Stéphane; Karimi, Ebrahim; Malomed, Boris A.; Seletskiy, Denis V.

This publication could be one of several versions: author's original, accepted manuscript or the publisher's version. / La version de cette publication peut être l'une des suivantes : la version prépublication de l'auteur, la version acceptée du manuscrit ou la version de l'éditeur.

For the publisher's version, please access the DOI link below./ Pour consulter la version de l'éditeur, utilisez le lien DOI ci-dessous.

Publisher's version / Version de l'éditeur:

https://doi.org/10.1002/lpor.202401714

Laser & Photonics Reviews, 19, 8, 2025-01-14

NRC Publications Archive Record / Notice des Archives des publications du CNRC :

https://nrc-publications.canada.ca/eng/view/object/?id=1106fba8-4f99-46df-9c0e-09777855de5a

https://publications-cnrc.canada.ca/fra/voir/objet/?id=1106fba8-4f99-46df-9c0e-09777855de5a

Access and use of this website and the material on it are subject to the Terms and Conditions set forth at https://nrc-publications.canada.ca/eng/copyright

READ THESE TERMS AND CONDITIONS CAREFULLY BEFORE USING THIS WEBSITE.

L'accès à ce site Web et l'utilisation de son contenu sont assujettis aux conditions présentées dans le site https://publications-cnrc.canada.ca/fra/droits

LISEZ CES CONDITIONS ATTENTIVEMENT AVANT D'UTILISER CE SITE WEB.

Questions? Contact the NRC Publications Archive team at PublicationsArchive-ArchivesPublications@nrc-cnrc.gc.ca. If you wish to email the authors directly, please see the first page of the publication for their contact information.

Vous avez des questions? Nous pouvons vous aider. Pour communiquer directement avec un auteur, consultez la première page de la revue dans laquelle son article a été publié afin de trouver ses coordonnées. Si vous n'arrivez pas à les repérer, communiquez avec nous à PublicationsArchive-ArchivesPublications@nrc-cnrc.gc.ca.

National Research Council Canada | Conseil national de recherches Canada

Canada

Check for updates

RESEARCH ARTICLE

LASER & PHOTONICS REVIEWS

www.lpr-journal.org

Experimental Emulator of Pulse Dynamics in Fractional Nonlinear Schrödinger Equation

Shilong Liu, Yingwen Zhang, Stéphane Virally, Ebrahim Karimi, Boris A. Malomed, and Denis V. Seletskiy**

A nonlinear optical platform is presented to emulate a nonlinear *Lévy waveguide* that supports the pulse propagation governed by a generalized fractional nonlinear Schrödinger equation (FNLSE). This approach distinguishes between intra-cavity and extra-cavity regimes, exploring the interplay between the effective fractional group-velocity dispersion (FGVD) and Kerr nonlinearity. In the intra-cavity configuration, stable *fractional solitons* enabled by an engineered combination of the fractional and regular dispersions in the fiber cavity are observed. The soliton pulses exhibit their specific characteristics, *viz.*, "heavy tails" and a "spectral valley" in the temporal and frequency domain, respectively, highlighting the effective nonlocality introduced by FGVD. Further investigation in the extra-cavity regime reveals the generation of spectral valleys with multiple lobes, offering potential applications to the design of high-dimensional data encoding. To elucidate the spectral valleys arising from the interplay of FGVD and nonlinearity, an innovative "force" model supported by comprehensive numerical analysis is developed. These findings open new avenues for experimental studies of spectral-temporal dynamics in fractional nonlinear systems.

1. Introduction

The fractional nonlinear Schrödinger equation (FNLSE) has attracted much interest due to its potential implementations in fractional quantum mechanics and nonlinear fractional physics.[1–4] Within this framework, a particularly interesting topic is the study of the pulse (quasi-soliton) dynamics governed by FNLSE, where the fundamentally novel feature is to address the fractional derivative in the governing equations.[5–7] The effective nonlocality introduced by the fractional derivative results in novel modal shapes, such as the fractional solitons,[8] which essentially expands the traditional concept of self-trapping and solitary waves. Different from the traditional solitons that are secured by the balance between the usual (non-fractional) dispersion and nonlinearity,[9] fractional solitons are stabilized by the interplay of the nonlinearity with the fractional nature of dispersion. The fractional solitons usually feature pronounced "heavy tails," thus enhancing the interaction range beyond the immediate vicinity of the waveforms.[8,10,11] Many numerical works have revealed diverse modes predicted by FNLSE, including fractional gap solitons,[12] vortex,[13] quadratic,[14] and spin-orbit coupling.[15] In addition, non-trivial beam propagation dynamics were studied within FNLSE, such as breathers,[3,16,17]

S. Liu
femtoQ Lab, Department of Engineering Physics
Polytechnique Montréal
Montréal, QC H3T 1J4, Canada
E-mail: shilong.liu@polymtl.ca

S. Liu
Tempo Optics Inc.
Montréal, QC H3T 1W9, Canada

Y. Zhang, E. Karimi
Department of Physics
University of Ottawa
25 Templeton, Ottawa, ON K1N 6N5, Canada

Y. Zhang, E. Karimi
National Research Council of Canada
100 Sussex Drive, Ottawa K1A0R6, Canada

S. Virally, D. V. Seletskiy
femtoQ Lab, Engineering Physics Department
Polytechnique Montréal
Montréal, QC H3T 1J4, Canada
E-mail: denis.seletskiy@polymtl.ca

B. A. Malomed
Department of Physical Electronics
Faculty of Engineering, and Center for Light-Matter Interaction
Tel Aviv University
Tel Aviv 69978, Israel

B. A. Malomed
Instituto de Alta Investigación
Universidad de Tarapacá, Arica
Casilla 7D, Chile

The ORCID identification number(s) for the author(s) of this article can be found under https://doi.org/10.1002/lpor.202401714

© 2025 The Author(s). Laser & Photonics Reviews published by Wiley-VCH GmbH. This is an open access article under the terms of the Creative Commons Attribution-NonCommercial License, which permits use, distribution and reproduction in any medium, provided the original work is properly cited and is not used for commercial purposes.

DOI: 10.1002/lpor.202401714

symmetry-breaking,[18–21] bifurcations,[22,23] and frequency conversion.[24]

In spite of the extensive theoretical developments, experimental implementation of pulse dynamics in fractional nonlinear systems remains a challenge. The main difficulty is to find a nonlinear *Lévy waveguide* (LW), which could implement the effect of both fractional group-velocity dispersion (FGVD) and nonlinearity. Recently, we have reported the realization of a linear optical LW in the spectral-temporal domain, where the FGVD is determined by an adjustable *Lévy index* (LI), $\alpha \in [0, 2]$.[25] By applying a fractional dispersion phase through a pulse shaper system, unique pulse dynamics, such as pulse splitting and merging, were observed within the framework of the fractional Schrödinger equation (FSE). This result suggests the possibility of using the ubiquitous Kerr nonlinearity of optical materials and FGVD to emulate nonlinear LWs.

In this work, we engage a pulse shaper to the fiber laser cavity, building a nonlinear LW to emulate the pulse dynamics governed by FNLSE. We establish two distinct operational regimes, intra- and extra-cavity ones. In the intra-cavity regime, we observe fractional solitons due to the main interplay of the FGVD and Kerr nonlinearity. We thus identify a stability boundary, determined by the FGVD length and LI. Typically, a valley is observed in the spectrum of the fractional solitons. To further investigate and enhance the spectral valley, we implement an extra-cavity regime, in which we can adjust both the FGVD and nonlinear strength. Furthermore, we have designed a segmented fractional phase profile in the initial pulse, which makes it possible to produce a spectral valley with multiple spectral lobes in the extra-cavity regime. The pulse shaper used in the current setup is also an efficient tool for performing spectral-temporal shaping in the linear pulse shaper settings,[26–28] supercontinuum tailoring,[29,30] as well as photonic-AI.[31,32]

The spectral valley is a typical feature resulting from the interplay between the FGVD and nonlinearity. Similar behavior was observed in the presence of regular (non-fractional) GVD and nonlinearity, in the form of self-phase modulation (SPM). These structures are crucially important for the formation of soliton pairs,[33–35] high-order soliton,[9,36,37] spectral-temporal pulse shaping,[38–43] spatial-temporal beam coupling,[44,45] supercontinuum generation[29] and few-cycle laser.[46,47] They are also observed in self-similar and fractal patterns.[48–51] In these contexts, the progression in the number N of the generated spectral lobes follows a *cascading* sequence with increasing nonlinearity, such as $1 \to 2 \to \cdots \to N$, determined by the accumulated nonlinear phase shift $\approx (N - 0.5)\pi$.[9,39] In contrast, the spectral valleys reported in the present work are connected by a sequence of *direct* transitions at the same level of nonlinearity, i.e., $1 \to N$, which is an advantage of the reported scenario. These spectral-valley modes are demonstrated to be efficient for implementing high-dimensional data encoding.

2. Pulse Dynamics in FNLSE (Fractional Nonlinear Schrödinger Equation)

The generalized FNLSE for a slowly-varying amplitude $\Psi(z, t)$ of the optical pulse propagating in the nonlinear LW is[25,52]

$$i\frac{\partial \Psi}{\partial z} = \left[\frac{D}{2}\left(\frac{-\partial^2}{\partial t^2}\right)^{\frac{\alpha}{2}} + \frac{\beta_2}{2}\frac{\partial^2}{\partial t^2} + i\frac{g}{2}\right]\Psi - \gamma|\Psi|^2\Psi, \tag{1}$$

where z and t are the propagation distance and reduced time,[9,29] respectively. On the right-hand side, the first term is the fractional (Riesz) time derivative,[25,53] with LI α and coefficient D. The second term represents the usual second-order GVD with coefficient β_2. g represents the gain coefficient, and γ defines the strength of the SPM nonlinearity.

The Riesz derivative is defined, with the help of the Fourier transform, as the nonlocal operator acting in the temporal domain:

$$\left(\frac{-\partial^2}{\partial t^2}\right)^{\frac{\alpha}{2}}\Psi(t) = \frac{1}{2\pi}\int_{-\infty}^{+\infty}|\omega|^{\alpha}d\omega\int_{-\infty}^{+\infty}dt' e^{-i\omega(t-t')}\Psi(t'). \tag{2}$$

The split-step algorithm can be used to solve the generalized FNLSE (Equation (1)). Regarding the dispersion part, the equation for marching from the segment n to $n + 1$ is

$$\tilde{\Psi}_{n+1}(\omega, z + \Delta z) = \tilde{\Psi}_n(\omega, z)\ \exp\left[-i\frac{D}{2}|\omega|^{\alpha}\Delta z + i\frac{\beta_2}{2}\omega^2\Delta z\right]. \tag{3}$$

The nonlinearity effect of SPM is implemented as

$$\Psi_{n+1}(t, z + \Delta z) = \Psi_n(t, z)\ \exp\left(iBI(t)\right), \tag{4}$$

where $B = \gamma P_k \Delta z$ represents the phase contribution from SPM. $I(t)$ represents the normalized temporal intensity (TI) of the pulse; γ and P_k indicate the Kerr coefficient and the peak power, respectively.

Based on this model, the pulse propagation in the nonlinear LW is determined by both regular and fractional GVD and SPM. Three cases are considered in the setting which makes it possible to neglect the linear gain: (i) the regular NLSE which does not include the fractional GVD ($D = 0$); (ii) the pure FNLSE which does not include regular GVD ($\beta_2 = 0$); and (iii) the generalized FNLSE which includes both the regular and fractional GVDs.

In case (i), NLSE has commonly known solutions for fundamental and higher-order solitons.[9] In case (ii), pure FNLSE supports stable pure "fractional soliton" solutions for $\alpha \in (1, 2)$.[4] In case (iii), the generalized FNLSE can support more complex solutions combining fractional and regular dispersion.

To obtain the solution for the fractional soliton, we consider the initial pulse with a *Lévy distribution* as $\Psi(t, z = 0) = \mathcal{L}_{\alpha',\gamma}(t)$,

$$\mathcal{L}_{\alpha',\gamma'}(t) = \frac{1}{\pi}\int_0^{\infty} e^{-\gamma' q^{\alpha'}}\cos(tq)dq, \tag{5}$$

where $\gamma' > 0$ and $\alpha' \in (0, 2]$. For $\alpha' = 1$, the distribution is equivalent to the classical Cauchy distribution, and for $\alpha' = 2$, it is tantamount to the Gaussian distribution but with fatter tails.[54]

Figure 1a displays the pulse dynamics for the pure FNLSE with $\alpha = 1.2$ by setting $\alpha' = \alpha$, which does not include regular GVD,

© 2025 The Author(s). Laser & Photonics Reviews published by Wiley-VCH GmbH

18638899, 2025, 8, Downloaded from https://onlinelibrary.wiley.com/doi/10.1002/lpor.202401714 by National Research Council, Wiley Online Library on [14/05/2025]. See the Terms and Conditions (https://onlinelibrary.wiley.com/terms-and-conditions) on Wiley Online Library for rules of use; OA articles are governed by the applicable Creative Commons License

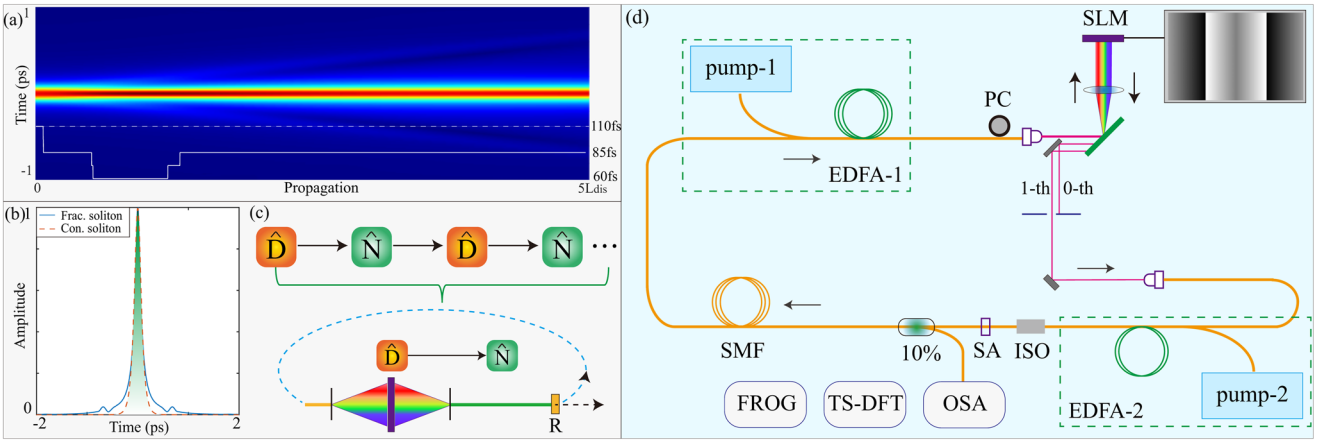

Figure 1. Simulations for the pulse dynamics in the framework of FNLSE, and its implementation in optics. a) The pulse-intensity evolution in five FDLs, where the initial pulse is set to be a Lévy distribution, $A \cdot \mathcal{L}_{1.2,1}(t/T_0)/|\mathcal{L}_{1.2,1}(t/T_0)|$, see Equation (5). Here, T_0 is 60.1 fs, $A = 18.76$, and $\alpha = 1.2$. The inserted fragmented white line shows the half-pulse width, which is 85 fs in the output. b) The final pulse amplitude for the produced fractional soliton with $\alpha = 1.2$ and the conventional soliton (the dashes red profile) are displayed for comparison. c) The scheme for the implementation of FNLSE in optics: the extra-cavity setup ($R = 0$), and the intra-cavity one ($R > 0$). d) The experimental setup of the intra-cavity is designed to emulate FNLSE. Here the labels are defined as follows: pump-1(2): the pump laser operating at 980 nm; EDFA-1(2): erbium-doped fiber amplifiers; PC: the polarization controller; SLM: the spatial light modulator; ISO: the fiber isolator; SA: the saturable absorber; SMF: the single-mode fiber.

over the propagation distance equivalent to five fractional dispersion lengths (FDL), with FDL defined as

$$L_{\alpha,\mathrm{FDL}} = \frac{2T_0^{\alpha}}{|D|^{\alpha}}, \quad \alpha \in (0, 2], \tag{6}$$

where T_0 is the duration of the initial pulse. More details about the FDL are shown in Section S1 (Supporting Information). The initial pulse with the Lévy distribution defined in (5), eventually forms a stable solution, as evidenced by monitoring its energy and pulse width. The blue solid line in Figure 1b represents the final fractional soliton pulse, which exhibits the feature of heavy tails. For reference, the dashed line shows the conventional soliton shaper, sech(t), as produced by the regular NLSE.

Realizing the pure FNLSE poses challenges in the experiment, while achieving a generalized FNLSE, as defined by (1), is more feasible. The cavity periodically applies transformations $\hat{D}$ and $\hat{N}$, induced by the GVD and nonlinearity, respectively, to the laser pulse circulating in the cavity, as shown in Figure 1c, thereby creating an effective fractional nonlinear system which governs the pulse evolution. This process is similar to generating "split-step solitons"[55] and "pure-quartic solitons."[56] In the weak dispersion regime, the pulse evolution may be approximated by a single-pass structure.[9] Thus, this setup operates in the "extra-cavity" regime ($R = 0$), as opposed to the "intra-cavity" one ($R > 0$), as shown in Figure 1c.

In our demonstration, we emulate the nonlinear LW using the mode-locked fiber laser (MLFL) and pulse shaper. In the "intra-cavity" configuration, the pulse shaper is placed inside the cavity to provide and maintain both regular and fractional dispersion, while the optical fiber and amplifier induce nonlinearity. In the "extra-cavity" configuration, the pulse shaper is moved outside the cavity, to act on the soliton pulse from MLFL. This configuration allows independent control of the action of the FGVD and nonlinearity on the incident pulse. In the experiments, we observed a stable fractional soliton pulse produced by the MLFL, demonstrating the efficiency of this approach to emulating pulse dynamics described by the generalized FNLSE.

3. Results

3.1. Intra-Cavity Regime: Fractional Soliton

Figure 1d shows the intra-cavity setup, which divides the cavity into free-space and in-fiber sections. The free-space one incorporates a 4f pulse shaper, equipped with a Spatial Light Modulator (SLM) that is loaded with a regular and fractional phase, as defined in (3). SLM is responsible for inducing the fractionality in the cavity, by imparting the corresponding phase shift to the passing pulse utilizing a properly designed hologram (schematically shown on the right-hand side of SLM in Figure 1d), as previously realized in the linear system.[25] The fiber component consists of two identical Er-doped fiber amplifiers (EDFA) and a single-mode fiber (SMF), which enhance the pulse energy and furnish the nonlinearity and regular dispersion. A saturable absorber (SA) is inserted into the fiber cavity to provide the saturation necessary for stable mode-locking. The output coupler diverts ≈ 10% of the pulse energy for monitoring purposes. The net dispersion in the cavity is ~ –0.12 ps^2, which ensures that the system readily produces the conventional soliton.[35,57] For diagnostics, we employ Frequency-Resolved Optical Gating (FROG) and an Optical Spectrum Analyzer (OSA) to measure the temporal and spectral profiles, respectively. Additionally, a Time-Stretch Dispersive Fourier Transform (TS-DFT) system is used to assess the pulse-by-pulse stability of the generated pulse train.

Figure 2a presents the spectral-temporal analysis of the fractional solitons produced in the intra-cavity setup, highlighting the effect of FGVD, as defined by two key parameters: LI (α) and dispersion distance L_{dis}. To explore their effects on the output soliton, α was varied from 0 to 2, and L_{dis} ranges from 0 to 150 m, with a fixed dispersion coefficient D of -21×10^{-3} ps$^{\alpha}$/m. Typically, when the flat phase ($[\alpha, L_{\mathrm{dis}}] = [0, 0]$) is loaded into the pulse

© 2025 The Author(s). Laser & Photonics Reviews published by Wiley-VCH GmbH

18638899, 2025, 8, Downloaded from https://onlinelibrary.wiley.com/doi/10.1002/lpor.202401714 by National Research Council, Wiley Online Library on [14/05/2025]. See the Terms and Conditions (https://onlinelibrary.wiley.com/terms-and-conditions) on Wiley Online Library for rules of use; OA articles are governed by the applicable Creative Commons License

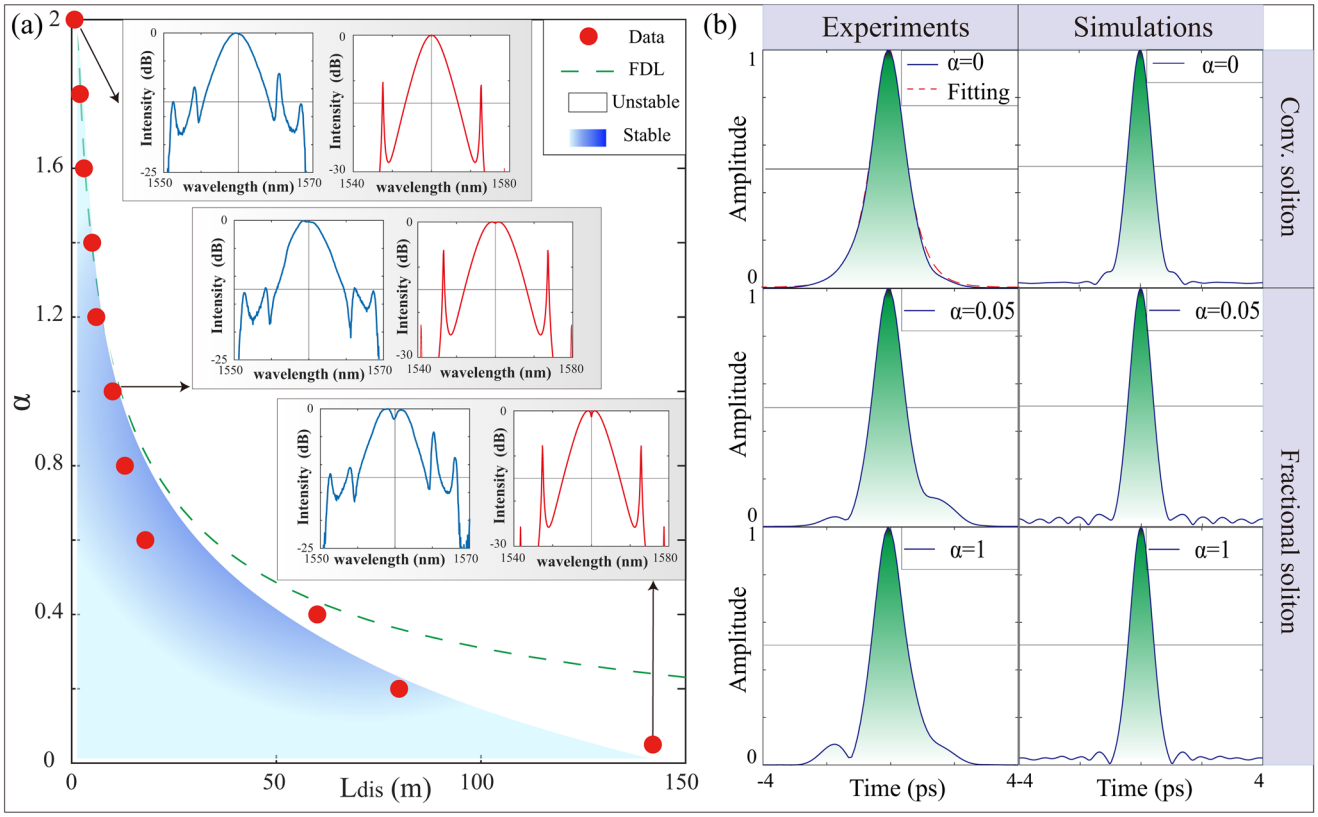

Figure 2. Spectral-temporal analysis of the soliton pulses produced by the mode-locked fiber laser. a) The stability analysis produced by varying LI (α) and dispersion length (L_{dis}). Data points indicate the boundary between stable and unstable soliton states; the dashed line represents the fractional-dispersion length (FDL) for $T_0 = 250$ fs. Insets show the measured and simulated (left and right sides, respectively) spectra for specific parameter settings: [α, L_{dis}] = [0,0], [1,10 m], and [0.05,142 m], respectively. b) The comparison of the pulse amplitude produced by the experiment and simulations. The experimental profiles were reconstructed by the FROG system.

shaper (PS), the cavity produces stable conventional solitons. The spectrum of this configuration is shown in the upper left panel, and the corresponding spectrum produced by the simulations is shown in the right panel. The simulation method for the setup is similar to one employed in our studies of the "soliton molecules" (bound states of solitons) in the fiber laser cavity[35] (**also see more details below in Experimental Section**).

The experimental and simulated spectra for the fractional-phase settings with [$\alpha = 1$, $L_{dis} = 10$ m] and [$\alpha = 0.05$, $L_{dis} = 142$ m] are shown in the middle and lower parts of Figure 2a, respectively. Compared to the traditional solitons, the fractional ones exhibit significant spectral alterations (most notably, a dip at the spectrum's center), modifying the pulse profile. To examine their temporal intensity, we employed the FROG system to reconstruct the spectral-temporal profiles. Figure 2b presents the so reconstructed temporal profiles. The top left panel exhibits the intensity of the conventional soliton, with the sech(T) shape, as indicated by the fitting dashed line. In contrast, two subsequent panels show the fractional pulses for the settings with [$\alpha = 1$, $L_{dis} = 10$ m] and [$\alpha = 0.05$, $L_{dis} = 142$ m], respectively. The characteristic "heavy tails" of the pulses are clearly observed.

The observed modifications are supported by simulations displayed in the right panels. This characteristic behavior is also observed for $\alpha \in (1, 2)$; additional results reconstructed by the FROG measurements can be found in Section S2 (Supporting Information). These features are emblematic of fractional solitons, being consistent with the characteristics reported in previous theoretical studies.[8,58,59]

Based on Figure 2a, for given LI α, it is observed that the output remains stable as L_{dis} increases, up to a certain threshold value beyond which the cavity becomes unstable. The reason is that larger L_{dis} induces the larger FGVD, leading to exceeding the temporal window of the PS and thus producing a distortion in the pulse profile.[28] In Figure 2a, the left blue area represents stability regions for the measured soliton pulse, while the right blank area indicates instability, where a robust spectrum does not form. The stability boundary aligns with the variation of the FGVD length as defined above and is shown here by the green dashed line.

A noteworthy feature revealed by the experiments is that the stability range of the output fractional soliton pulses extends, in terms of LI α, from 0 to 2. In contrast, the predicted stability area for the pure FNLSE is found for α between 1 and 2, as it gives rise to the collapse at $\alpha \leq 1$.[4] The reason for this difference is that the constructed cavity is not a pure FNLSE system, as it also incorporates regular GVD and other effects, such as saturable absorption. These effects help to suppress the destabilizing factor of the collapse and extend the stability area to $\alpha \leq 1$. As a result, the current intra-cavity system is closer to the generalized FNLSE model.

© 2025 The Author(s). Laser & Photonics Reviews published by Wiley-VCH GmbH

18638899, 2025, 8, Downloaded from https://onlinelibrary.wiley.com/doi/10.1002/lpor.202401714 by National Research Council, Wiley Online Library on [14/05/2025]. See the Terms and Conditions (https://onlinelibrary.wiley.com/terms-and-conditions) on Wiley Online Library for rules of use; OA articles are governed by the applicable Creative Commons License

3.2. The Extra-Cavity FNLSE-Emulating Regime: Spectral Valleys

Limited by the stability boundary in the intra-cavity regime, as illustrated in Figure 2a, the cavity is not stable for the larger FGVD, and thus the depth of the spectral dip cannot be made more pronounced. To circumvent this limitation, we ran the experiments with the extra-cavity regime. For this purpose, we relocated the PS outside the cavity and incorporated an EDFA to control the nonlinearity strength, by varying the EDFA's pump power from 70 to 350 mW. In this regime, the pulse shaper is used to change the effects of both the regular and fractional GVD on the initial pulse. The extra-cavity setup offers the flexibility to alter the initial conditions and nonlinearity. Technical details concerning the extra-cavity setup are available in Section S3 (Supporting Information).

We initially maintain the pump power in EDFA of 70 mW and manipulate the initial spectral phase by dint of the PS. The primary spectral phase is flat, denoted as $[\alpha = 0, L_{\text{dis}} = 0]$. In this configuration, the soliton pulse passes through the PS without additional spectral modulations. We conducted FROG measurements on the initial soliton pulse. The reconstructed pulse duration T_0 is $\approx$ 810 fs, with the reconstructed spectral phase approximately following the second-order distribution $\sim \omega^2$, which corresponds to the second-order GVD. This phase pattern results from the effects of the fibers and optical elements in the setup, which can be compensated by adding an opposite second-order spectral phase in the pulse shaper. Our tests indicate that the pulse duration is minimized at the value of $\approx$ 352 fs when the compensating GVD phase corresponds to the dispersion length times a factor $\approx$ 1.7 (More details are produced in Section S4, Supporting Information).

The next step involves fixing the spectral phase and recording the spectral intensity (SI) by varying the pump power, i.e., effectively changing the value of B in Equation 4. **Figure 3a1,2** display the recorded SI for the initial pulse produced by PS with regular GVD. In Figure 3a1, the SPM-induced variations in SI are weak, due to the stretched pulse induced by the offset GVD of the attached single-mode fiber. If the offset GVD is compensated, hence the pulse duration is minimized, the SPM effect becomes evident, as shown in Figure 3 a2. Here, the interference dip emerges around 290 mW, corresponding to $B \approx 1.55\pi$ (**The relation between the pump power and** B is presented in Section S3, Supporting Information).

As per the relationship between the number of lobes and the maximum phase shift $(N - 0.5)\pi$,[9] the theoretical value of B in Figure 3 a2 should be 1.5π. However, this threshold can be lowered when the initial pulse is modulated by fractional GVD. For instance, Figure 3 a3,4 shows the recorded SI for the loading phase with parameters $[\alpha = 1, L_{\text{dis}} = 2.42L_{\alpha,\text{FDL}}]$ and $[\alpha = 0.2, L_{\text{dis}} = 0.88L_{\alpha,\text{FDL}}]$, respectively, revealing a pronounced dip even at lower pump powers, 280 mW ($B = 1.46\pi$) and 240 mW ($B = 1.11\pi$), respectively. As α decreases, the deepest dip occurs at smaller values of B. Insets in these panels show the recorded spectra for the pump power fixed at 240 mW, highlighting the enhancement in the pronounced dips induced by fractional GVD. Moreover, the corresponding reconstructed temporal intensity (TI) for the pump 240 mW is shown at the bottom of Figure 3 a1–4, highlighting the profiles induced by fractional GVD, with the "heavy tails."

The observed spectrum displays a distinctive dip, which suggests the name of "spectral valley" to this feature. We designate the spectral valley by the symbol {N}. In particular, {N = 2} means that the spectrum has two peak lobes and one valley, as shown in Figure 3 a3,4. It is possible to produce the spectral valley with multiple lobes (N > 2) by designing a phase structure that incorporates multiple fractional segmented phases. Note that a Kelly sideband in soliton pulses causes crosstalk in the spectrum, which was eliminated by integrating a bandpass filter (see details in Section S5, Supporting Information).

To explain the observed spectral valley {N}, we proposed a "force" model by addressing the frequency chirp. Three effective forces are referred to as "attraction," "repulsion," and "equilibration." By employing the force model, one can design the segmented phase to produce the spectral valley of the {N} type. Details of the force model are shown below in **Experimental Section**.

The required fractional spectral phase patterns, wrapped between $-\pi$ and $+\pi$, are shown at the top of Figure 3 b1–4. To generate the spectral valley of {2}, we set FGVD to have LI $\alpha = 1$:

$$\alpha = 1,\ L_{\text{dis}} = 3.87 \times L_{\alpha,\text{FDL}} \tag{7}$$

Using the so-designed fractional phase, we have obtained the experimental SI by varying the pump power, as shown in Figure 3 b1. At the pump power of $\approx$ 250 mW, two distinct peaks are observed in the spectrum. Figure 3 c1 presents the spectrum versus B, as obtained from the simulations of FNLSE (**see simulations in Experimental Section**).

To create the spectral valley {3} with three lobes, the segmented spectral phase can be designed to carry a fractional and constant term, based on the force model:

$$\begin{cases} \alpha = 0, L_{\text{dis}} = 0 & |\lambda - \lambda_c| <= 1.5\ \text{nm} \\ \alpha = 1\ , L_{\text{dis}} = 3.15 \times L_{\alpha,\text{FDL}} & \text{otherwise} \end{cases} \tag{8}$$

where λ_c is the central wavelength. Adding a global GVD phase to this segmented phase pattern yields the final phase configuration, showcased in the top plot of Figure 3 b2. When this phase is imposed on SLM, three lobes are formed in SI with the increase of the pump power, as displayed in Figure 3 b2, and by simulations in Figure 3 c2, respectively. Notably, three lobes emerge in both cases even for relatively small values of B. As the pump power increases further, the two side lobes retain greater intensity than the central one, subsequently fading out due to interference effects. This behavior aligns with the force model, where the unique phase distribution contributes to the emergence of three lobes: the lateral lobes are generated by the repulsive force, while the central segment preserves the original state due to the equilibration.

Figure 3b3–c3 illustrates the scenario with the spectral valley {4}, produced by dividing the phase configuration into four segments, based on their effective-force interactions. This design involves two fractional terms with LIs $\alpha = 0.5$ and 1, respectively. Notably, the total force exerted by the segment with $\alpha = 0.5$ must be weaker than that produced by the segment with $\alpha = 1$. Thus, the required fractional GVD phase is expressed as follows:

$$\begin{cases} \alpha = 0.5,\ L_{\text{dis}} = 0.79 \times L_{\alpha,\text{FDL}} & |\lambda - \lambda_c| \le 2\ \text{nm} \\ \alpha = 1,\ L_{\text{dis}} = 3.57 \times L_{\alpha,\text{FDL}} & \text{otherwise} \end{cases} \tag{9}$$

© 2025 The Author(s). Laser & Photonics Reviews published by Wiley-VCH GmbH

18638899, 2025, 8, Downloaded from https://onlinelibrary.wiley.com/doi/10.1002/lpor.202401714 by National Research Council, Wiley Online Library on [14/05/2025]. See the Terms and Conditions (https://onlinelibrary.wiley.com/terms-and-conditions) on Wiley Online Library for rules of use; OA articles are governed by the applicable Creative Commons License

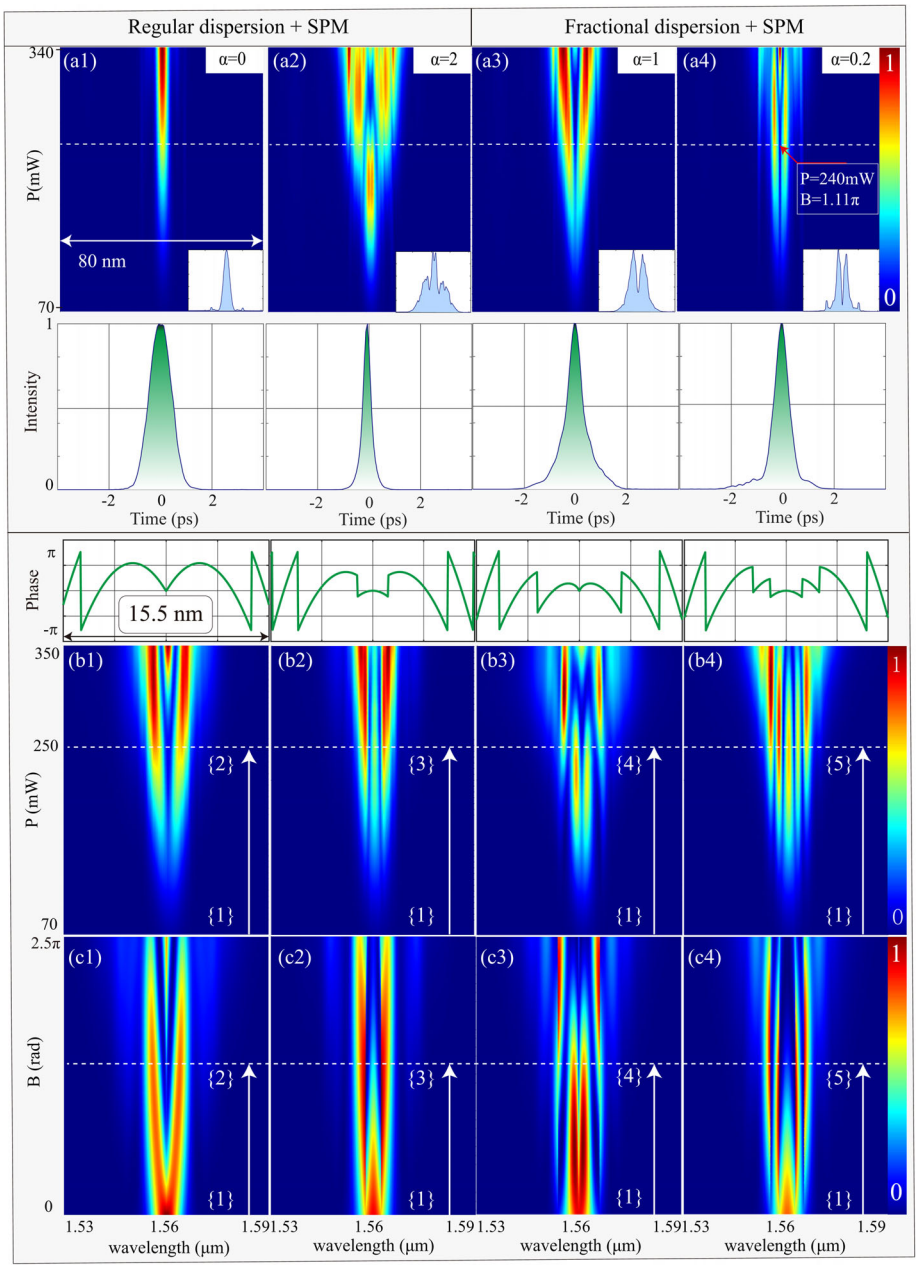

Figure 3. Spectral responses to varying the EDFA's pump power in the extra-cavity regime. (a1–4): Recorded spectra produced by the flat [$\alpha = 0$, $L_{dis} = 0$], second-order [$\alpha = 2$, $L_{dis} = 1.7L_{\alpha,FDL}$], fractional-order [$\alpha = 1$, $L_{dis} = 2.42L_{\alpha,FDL}$] and [$\alpha = 0.2$, $L_{dis} = 0.88L_{\alpha,FDL}$] GVD, respectively. The bottom panels show the temporal intensity reconstructed by the FROG system for the pump power in 240 mW. (b1–4): Showcasing the spectral valleys with multiple lobes, under the action of the segmented fractional phase, as indicated at the top of each panel and defined in Equations (7)–(10), respectively. (c1–4): The corresponding spectra, as obtained in the simulations.

Upon applying the required spectral phase to the initial pulse, a four-lobe pattern emerges within the pump power range of 70 – 250 mW. Due to interference effects, the two central lobes disappear but may reappear with a further increase of the pump power. We do not show results for still higher powers because of the plausible occurrence of the gain saturation in that case.[60]

More lobes can be realized by partitioning the fractional phase into more segments. This entails designing a multi-functional force distribution, encompassing attributes such as "equilibration," "weak repulsion," and "strong repulsion." To realize this, the spectral phase configuration is arranged as follows:

$$\begin{cases} \alpha = 0\ , L_{dis} = 0, & |\lambda - \lambda_c| <= 1.6\ \text{nm} \\ \alpha = 0.5\ , L_{dis} = 0.97 \times L_{\alpha,FDL}, & 1.6\ \text{nm} < |\lambda - \lambda_c| \leq 3.2\ \text{nm} \\ \alpha = 1\ , L_{dis} = 3.57 \times L_{\alpha,FDL}, & \text{others.} \end{cases} \tag{10}$$

The spectral phase defined in Equation (10) is displayed at the top of Figure 3 b4, where five segmented phases are observed.

© 2025 The Author(s). Laser & Photonics Reviews published by Wiley-VCH GmbH

18638899, 2025, 8, Downloaded from https://onlinelibrary.wiley.com/doi/10.1002/lpor.202401714 by National Research Council, Wiley Online Library on [14/05/2025]. See the Terms and Conditions (https://onlinelibrary.wiley.com/terms-and-conditions) on Wiley Online Library for rules of use; OA articles are governed by the applicable Creative Commons License

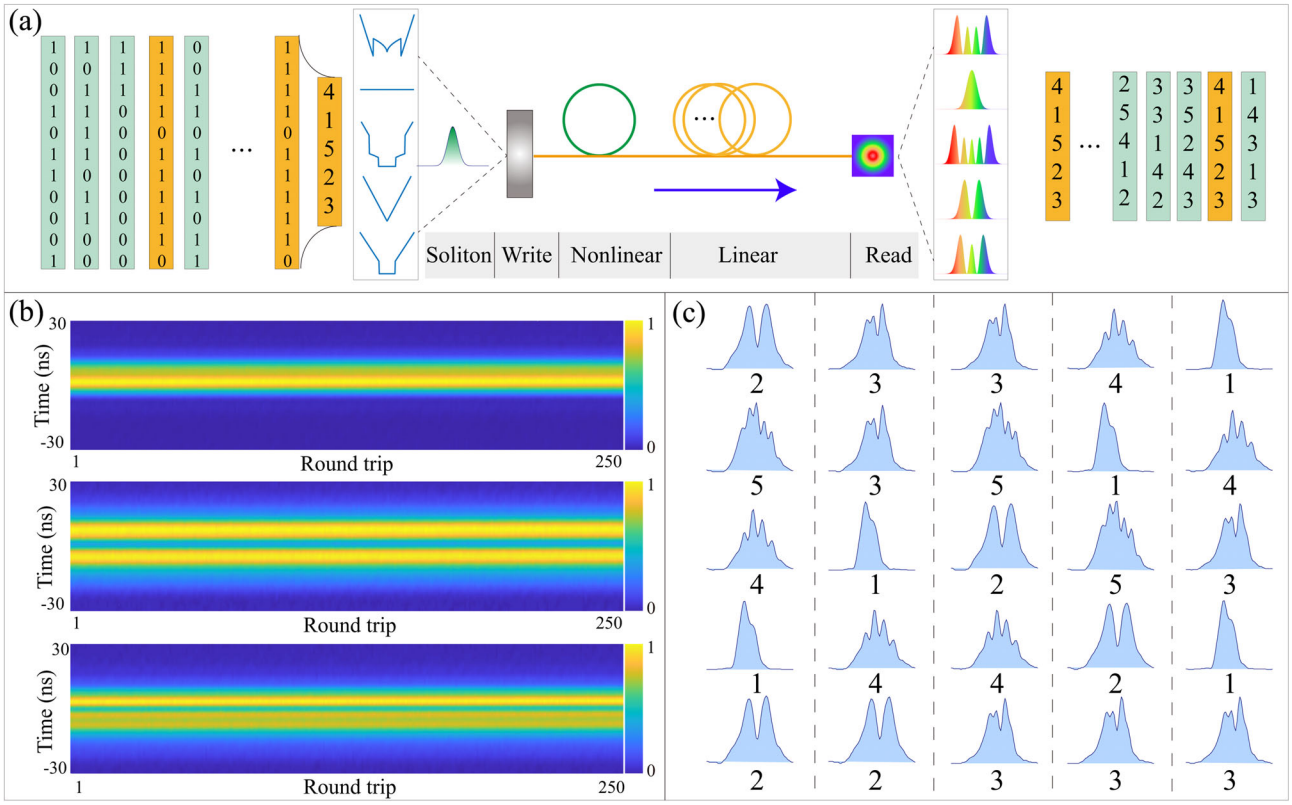

Figure 4. The application of the spectral valleys to high-dimensional data encoding. a) The pulse transmission regime for the data encoding from binary to quinary by using five spectral-valley modes. It includes a "soliton" pulse from a mode-locked fiber laser, the "write" section operated by a pulse shaper, a "nonlinear" SPM section, a "linear" fiber link of the length ≃ 100 km, and a "read" section including a photodetector and oscilloscope. b) Stretched temporal profiles recorded by the oscilloscope for modes of {1}, {2}, and {3}, respectively. c) The recorded temporal profiles of {25412, 33142, 35243, 4152, 14313} strings, as realized with 25 holograms and produced by the oscilloscope for one round trip.

Loading this phase into PS and subsequently altering the pump power results in SI variations, as displayed in Figure 3 b4. Experimental observations confirm that this segmented phase design induces a spectral valley with five lobes.

The simulations of SI (Figure 3 c1–4) maintain the conservation of the input pulse energy, which is consistent with the experimental settings. In the simulations and experiments alike, we introduced an additional second-orderGVD phase term, with the size corresponding to a factor ≈ 3.37 times the dispersion length, as a global phase for the designed fractional-GVD pattern. This global phase serves a dual purpose: it counterbalances the added dispersion, caused by the optical setup, and enhances the suitable temporal chirp for more pronounced interference, resulting in a deeper dip. Moreover, at the pump power level of ≈ 250 mW, the exact number of the lobes in the spectral valley can be found. This suggests a promising application for dense data encoding by using these spectral valley states, as shown in the next subsection.

3.3. The Applications of Spectral Valleys in High-Dimensional Data Encoding

In experimental results presented in Figure 3, two relevant features are observed. First, by adjusting the spectral phase suitably in the hologram inserted into SLM, spectral valleys with multiple lobes can be created. Second, these modes can be created with the same nonlinearity, or the same pump power, which is beneficial and convenient for high-dimensional encoding. Applying these spectral-valley modes to the optical signal transmission is a promising possibility. Traditional optical transmission systems usually use binary encoding, i.e., "0" or "1." However, creating five spectral-valley modes goes beyond the binary format, allowing a quinary one. **Figure 4** demonstrates high-dimensional encoding with the format rearranging from binary to quinary, by using five spectral valley modes {1} to {5}, where {1} stands for the fundamental mode without the spectral split.

To perform the data encoding, the first step is to transform the binary data into a quinary format, shown in the left part of Figure 4a. These quinary datasets ({25412, 33142, 35243, 41523, 14313}) are then encoded in sequence into the above-mentioned five spectral phases, which represent the "write" process. In the second stage, the pump power is fixed at around 250 mW, and the corresponding spectral-valley mode is generated under the action of SPM. The signal is then transmitted through ≈ 100 km of the fiber (labeled "linear" in Figure 4a) and registered by the photodetector and oscilloscope named the "read" section. Due to the effect of the group delay dispersion, induced by the long fiber, the stretched temporal profiles shown by the oscilloscope are proportional to

© 2025 The Author(s). Laser & Photonics Reviews published by Wiley-VCH GmbH

18638899, 2025, 8, Downloaded from https://onlinelibrary.wiley.com/doi/10.1002/lpor.202401714 by National Research Council, Wiley Online Library on [14/05/2025]. See the Terms and Conditions (https://onlinelibrary.wiley.com/terms-and-conditions) on Wiley Online Library for rules of use; OA articles are governed by the applicable Creative Commons License

the spectral intensity.[35,61,62] At the last stage, the peak numbers in these profiles are counted and the data is decoded back from quinary to binary.

Figure 4b shows the stretched temporal profiles recorded on the oscilloscope for the spectral valley modes {1}, {2}, and {3}, respectively. The stretched temporal profiles demonstrate robustness over 250 round trips and a dip is clearly observed at the center of the profile. Figure 4c shows one of the output profiles, with the above-mentioned complex phase encoded by 25 holograms. By counting the number of peaks in these profiles, we obtain the same sequence. It should be noted that the dips for the bifurcation modes of {3} to {5} are not very deep, in terms of limitations imposed by the sampling rate and temporal resolution of the oscilloscope. In addition, the higher-order GVD in the 100-km fiber affects the shape of these profiles. Nevertheless, the results demonstrate that the spectral valleys offer promising potential applications to optical signal processing, particularly for high-dimensional data encoding.

4. Conclusion

In this work, we have theoretically explored and experimentally studied a nonlinear LW (*Lévy waveguide*) in the laser-cavity configuration. The LW is modeled by the generalized FNLSE (fractional nonlinear Schrödinger equation), in which the pulse dynamics are determined by the interplay between FGVD (fractional group-velocity dispersion) and SPM (self-phase modulation). Our experiments conducted in the intracavity regime reveal the existence of robust fractional solitons featuring the characteristic "heavy tails" at pulse edges.

In addition, by implementing the extra-cavity scenario, we have built a single-pass regime to emulate the spectral-temporal dynamics governed by the generalized FNLSE. To explain the observed spectral valleys, we have developed an effective "force" model and performed its detailed analysis. With the help of the force model, we have designed fractional segmented phase patterns to produce multiple spectral valleys.

The multiple lobes of the spectral valleys realized in the current study highlight two primary advancements. First, due to the beneficial interplay between the FGVD and SPM, these lobes can be observed even in the case of weaker nonlinearity. In contrast, for purely nonlinear systems, where regular SPM dominates, multiple lobes typically require a much higher degree of nonlinearity to be noticeable.[9,39] Second, the lobes of the spectral valleys can be controlled on demand via the phase modulation, which offers a high-efficiency nonlinear shaping regime, in comparison with the linear pulse shaping methods by employing spectral amplitude modulations.[28,63] These advancements indicate that the spectral valleys observed in this work are promising for applications to optical data processing. Experimentally, we have demonstrated high-dimensional optical data encoding using five-spectral-valley states, successfully transmitting data over 100 km of the single-mode fiber. Recent advances also suggest the potential for developing a real-time signal processor with a capacity of up to 17 Tb s^{-1}, leveraging fractional-differentiation orders, which warrants further investigation.

Although the concept of the fractional derivative and dispersion has a long history, their realization in physical systems, such as nonlinear fiber optics, is a relatively new and emerging topic. This inspires several promising perspectives: 1) The immediate goal is to explore additional solutions of the FNLSE. The current results focus primarily on positive fractional dispersion lengths, corresponding to the "repulsion" case in the force model, which explains the observed spectral valleys. However, equally intriguing results are expected in the "attraction" case, which would illustrate spectral squeezing. Recently two works have demonstrated an "attraction" effect (narrowed spectrum) in similar contexts.[65,66] By involving additional parameters, such as higher-order dispersion or stronger nonlinearity, even greater diversity in the pulse dynamics could be uncovered. 2) The second perspective is the realization of the spatial-temporal light synthesis by incorporating both fractional dispersion and fractional diffraction. This approach has significant potential for applications to optical encoding and spatiotemporal mode-locked laser architectures.[67,68] 3) Finally, due to the mathematical similarity between the FNLSE in nonlinear optics and its quantum counterpart, this regime may serve as an effective model for emulating fractional quantum mechanics.[1,69]

Table 1. Simulation parameters for the intra-cavity regime.

Parameter	Value
Central wavelength, λ_c	1560 nm
Maximum frequency range, ω_m	54 ps^{-1}
Length of SMF, L_{SMF}	6.5 m
Dispersion of SMF, $\beta_{2,SMF}$	−21 ps^2 km^{-1}
Nonlinear coefficient of SMF, γ_{SMF}	0.0013 $W^{-1}m^{-1}$
Length of Er fiber, L_{Er}	2 m
Dispersion of Er fiber, $\beta_{2,Er}$	12.1 ps^2 km^{-1}
Nonlinear coefficient of Er, γ_{Er}	0.003 $W^{-1}m^{-1}$
Saturation energy, E_{sat}	40 pJ
Dispersion parameter, D	−21 ps^{α} km^{-1}
Small-signal gain, g_0	5.5 m^{-1}
Linear saturable absorption, α_0	0.095
Unsaturated absorption, α_{ns}	0.49
Saturation intensity, I_{sat}	21 MW cm^{-2}
Transmission rate, δ	0.2
Output coupling ratio, R_{out}	0.10
Effective cross-sectional area, A_{eff}	63.6×10^{-12} m^2

5. Experimental Section

Numerical Simulations for the FNLSE: To simulate the intracavity regime as shown in Figure 1d, three components were handled separately: NLSE for the fiber, FGVD for the pulse shaper, and the transfer function for SA (saturable absorber). For the fiber segments and EDFA, the governing equation is

$$i\frac{\partial \Psi}{\partial z} = \left(\frac{\beta_2}{2}\frac{\partial^2}{\partial t^2} + i\frac{g}{2}\right)\Psi - \gamma|\Psi|^2\Psi, \tag{11}$$

where the second-order dispersion was considered only, although high-order dispersion gives rise to more non-trivial results.[37,70] The gain parameter $g = g_0 \exp(-E(z)/E_{sat})$ for the erbium-doped fiber is determined by the small-signal gain g_0 and saturation energy E_{sat}. The total energy of the pulse is $E(z) = \int_{-\infty}^{+\infty} |\Psi(z,t)|^2\, dt$.

© 2025 The Author(s). Laser & Photonics Reviews published by Wiley-VCH GmbH

18638899, 2025, 8, Downloaded from https://onlinelibrary.wiley.com/doi/10.1002/lpor.202401714 by National Research Council, Wiley Online Library on [14/05/2025]. See the Terms and Conditions (https://onlinelibrary.wiley.com/terms-and-conditions) on Wiley Online Library for rules of use; OA articles are governed by the applicable Creative Commons License

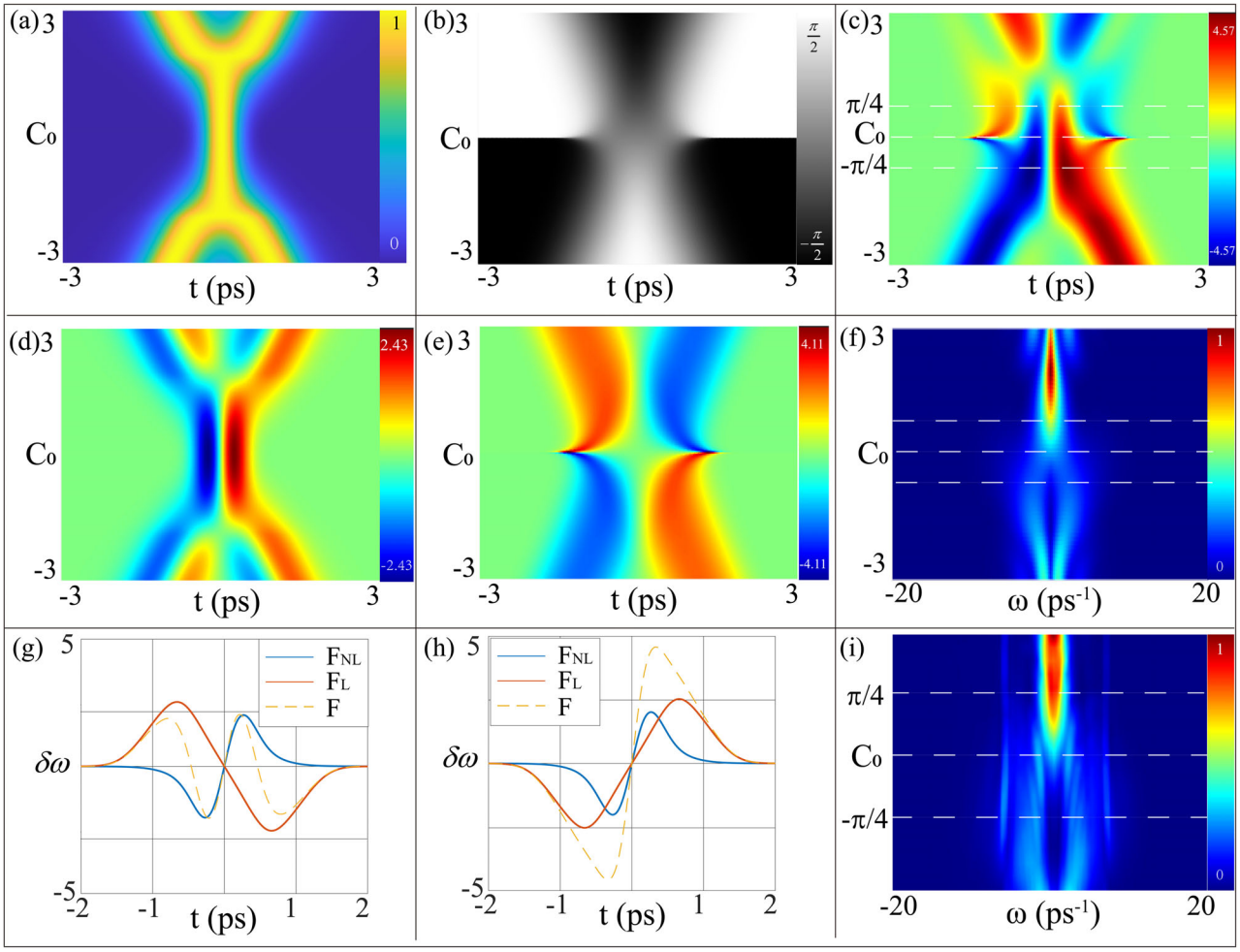

Figure 5. Simulations and experiments for pulse's spectra under the action of FGVD and nonlinearity. a,d) The normalized temporal intensity and gradient ($-\partial I/\partial t$). b,e) The corresponding temporal phase and gradient ($-\partial\phi/\partial t$). c) The summary effective force for $B = \pi/2$. f) The calculated spectral intensity for C_0 varying between −3 to +3. g,h) The calculated three forces for $C_0 = +\pi/4$ and $C_0 = -\pi/4$, respectively. i) The measured spectral intensity for C_0 varying from −1.8 to 1.8.

The pulse shaper, located in the free-space section of the cavity, is used to engineer the additional fractional or regular dispersion, which is modeled by the following map:

$$\tilde{\Psi}(\omega, L_{4f}) = \tilde{\Psi}(\omega, 0)\sqrt{\delta}\exp\left(\frac{iDL_{\alpha,\mathrm{dis}}|\omega|^{\alpha}}{2}\right)\mathrm{Rect}\left(\frac{\omega}{\omega_m}\right). \tag{12}$$

Here, $L_{\alpha,\mathrm{dis}}$ is the dispersion quantity for the given GVD order α including the fractional one(s), which is (are) characterized its (their) LI α, and L_{4f} is the overall length of the 4f pulse shaper. Parameter δ is the overall transmission coefficient, and $\alpha = 2$ represents the regular (non-fractional) GVD. Rect(x) is the filter function of the pulse shaper, where ω_m represents the maximum frequency range limited by the size of the SLM.

To achieve stable mode-locking, the setup also includes an SA based on carbon nanotubes, similar to the one introduced in ref. [35]. The absorber is characterized by its transfer function:

$$T_{\mathrm{ab}} = \sqrt{1 - (\alpha_{\mathrm{ns}} + \alpha_0/(1 + A^2/I_{\mathrm{sat}} \cdot A_{\mathrm{eff}}))}. \tag{13}$$

Here, α_{ns} is the unsaturated absorption, α_0 is the linear limit of the saturable absorption, I_{sat} is the saturation intensity, and A_{eff} is the effective cross-section area of the fiber.

Using Equations (11)–(13), the evolution of the pulse is simulated in the cavity. After approximately 100 round trips, the output pulse stabilizes, as verified by monitoring variations in its momentum and energy. To confirm the long-term stability, the maximum number of round trips is set to 1000, and the final spectral and temporal amplitude profiles are presented in Figure 2. The parameters used in these simulations are summarized in **Table 1**.

The simulations of the extra-cavity regime are similar, in which case Equation (12) is first used to imprint the initial spectral phase onto the incident pulse. Then, Equation (11) governs the propagation.

The Force Model to Explain the FGVD-SPM Interplay: The dynamics of the spectral valleys are similar to the oscillating structure induced by standard SPM. However, the unique feature observed in the present setting is the *direct* transitions from {1} to {N}, while, as mentioned above, solely *cascaded* transition sequences occur with the increase of the nonlinearity in the case of standard SPM. To study the FGVD-SPM interplay, the frequency chirp was focused,

$$\delta\omega(B, t) = -\frac{\partial[\phi_{NL}(t) + \phi_L(t)]}{\partial t} = F_{NL}(t) + F_L(t), \tag{14}$$

where $\phi_L(t)$ denotes the temporal phase induced by FGVD, and $\phi_{NL}(t)$ is the SPM-induced nonlinear phase. The derivatives $F_{NL}(t) =$

© 2025 The Author(s). Laser & Photonics Reviews published by Wiley-VCH GmbH

18638899, 2025, 8, Downloaded from https://onlinelibrary.wiley.com/doi/10.1002/lpor.202401714 by National Research Council, Wiley Online Library on [14/05/2025]. See the Terms and Conditions (https://onlinelibrary.wiley.com/terms-and-conditions) on Wiley Online Library for rules of use; OA articles are governed by the applicable Creative Commons License

$-\partial\phi_{NL}(t)/\partial t \equiv -B\partial I(t)/\partial t$ [see Equation (4)] and $F_L(t) = -\partial\phi_L(t)/\partial t$, which may be compared to the effective forces that induce the frequency shift in the input pulse,[71] are represented by the total effective force, $F(t)$. This picture gives rise to three distinct scenarios, which are defined as "repulsion" ($F(t) > 0$), "attraction" ($F(t) < 0$), and "equilibration," ($F(t) = 0$). In particular, the "repulsive" force leads to an increase in the frequency, akin to the blue shift of optical pulses.

To visualize the "force" under the action of FGVD with $\alpha = 1$, we consider the initial pulse with the Gaussian spectral shape, *viz.*,

$$\tilde{\Psi}(\omega) = \exp\left[-\left(\frac{\omega}{\Delta\omega}\right)^2 - iC_0|\omega|\right]. \tag{15}$$

Here, $\Delta\omega$ is the bandwidth and C_0 represents the strength of the fractional GVD. The respective temporal field can be written as

$$\Psi(t) = \mathcal{F}^{-1}\left[\tilde{\Psi}(\omega)\right] = \frac{\Delta\omega\sqrt{\pi}}{2}\left(E_n \cdot (1 - if_n) + E_p \cdot (1 - if_p)\right), \tag{16}$$

with

$$\begin{cases} f_n = \mathrm{erfi}\left(\frac{\Delta\omega(C_0 - t)}{2}\right), \\ f_p = \mathrm{erfi}\left(\frac{\Delta\omega(C_0 + t)}{2}\right), \\ E_n = \exp\left(-\frac{\Delta\omega^2(C_0 - t)^2}{4}\right), \\ E_p = \exp\left(-\frac{\Delta\omega^2(C_0 + t)^2}{4}\right), \end{cases} \tag{17}$$

where $\mathrm{erfi}(x) = \int_0^x \exp(\tau^2)d\tau$. Based on Equations (14) and (16), one can calculate the temporal phase induced by FGVD and the SPM-induced nonlinear phase, which makes it possible to obtain the force distributions, i.e., $F(C_0, t)$. The calculated normalized temporal intensity and phase are shown in **Figure 5**a,b, and the corresponding gradients are shown in Figure 5d,e, in which we set $\Delta\omega = 4\ \mathrm{ps}^{-1}$ and $B = \pi/2$.

By taking these findings into account, the total force $F(C_0, t)$ was obtained, which is shown in Figure 5c. It is clearly seen that two branches appear with a strong dip at $C_0 < 0$, which implies that the repulsive force creates a spectral valley. This conclusion is corroborated by the spectrum, as shown in Figure 5f (the simulation) and Figure 5(i) (the experiment). Specifically, Figure 5g,h shows the force distribution for $C_0 = +\pi/4$ and $-\pi/4$, respectively. In the latter case, the two forces have identical signs, enhancing the total "repulsion" force. On the other hand, the two forces almost cancel each other for $C_0 = +\pi/4$, showing the "equilibration."

Supporting Information

Supporting Information is available from the Wiley Online Library or from the author.

Acknowledgements

The authors would like to thank Prof. Ebrahim Karimi's SQO group for providing the spatial light modulator. The authors appreciate the following colleagues in Polytechnique Montréal for their help in experiments and discussions: Godbout Nicholas, Mikael Leduc, Sho Onoe, Laurent Rivard, Gabriel Demontigny, Patrick Cusson, Marco Scaglia, Émile Dessureault, Grégory-Samuel Zagbayou, Rodrigo Itzamna Becerra Deana, as well as Émile Jetzer. In particular, the authors thank Prof. Kai Wang's (McGill University) beneficial discussions on the results and the potential regimes, Chi Zhang's (Polytechnique Montréal) help in the design of the saturable absorber, as well as Prof. Yudong Cui's (Zhejiang University) discussions concerning mode-locked fiber lasers. In addition, the authors appreciate the assistance of Christine Tao (Tempo Optics Inc.) in the improvement of the figure quality. Natural Sciences and Engineering Research Council of Canada (NSERC) via the Canada Research Chair (CRC) of D.V.S.; the Fonds de Recherche du Québec Nature et Technologies (FRQNT) via Institut Transdisciplinaire d' Information Quantique Transdisciplinary Institute for Quantum Information (INTRIQ); PBEEE/Bourses de court séjour de recherche ou perfectionnement from FRONT; Canada Research Chair Program (CRC) of E. K., NRC-uOttawa Joint Center for Extreme Quantum Photonics (JCEP); Mitacs Accelerate Program; Israel Science Foundation via grant No. 1695/22 by B. A. M. European Union's Horizon Europe research and innovation programme under grant agreement No. 101070700 (project MIRAQLS).

Conflict of Interest

The authors declare no conflict of interest.

Data Availability Statement

The data that support the findings of this study are available from the corresponding author upon reasonable request.

Keywords

fractional nonlinear schrödinger equation, fractional soliton, mode-locked fiber laser, pulse shaper

Received: October 13, 2024
Revised: December 22, 2024
Published online: January 14, 2025

[1] N. Laskin, *Phys. Lett. A* **2000**, *268*, 298.
[2] S. Longhi, *Opt. Lett.* **2015**, *40*, 1117.
[3] Y. Zhang, X. Liu, M. R. Belić, W. Zhong, Y. Zhang, M. Xiao, *Phys. Rev. Lett.* **2015**, *115*, 180403.
[4] B. A. Malomed, *Chaos: An Interdisc. J. Nonlin. Sci.* **2024**, *34*, 2.
[5] A. Atangana, D. Baleanu, *arXiv preprint arXiv:1602.03408* **2016**.
[6] C. Y. Kee, L. Ang, *APL Quantum* **2024**, *1*, 1.
[7] Z. Chen, X. Liu, H. Xie, J. Zeng, *Chaos, Solitons Fractals* **2024**, *180*, 114558.
[8] J. Fujioka, A. Espinosa, R. Rodríguez, *Phys. Lett. A* **2010**, *374*, 1126.
[9] G. P. Agrawal, in *Nonlinear Science at the Dawn of the 21st Century*, Springer, **2000**, pp. 195–211.
[10] M. Chen, S. Zeng, D. Lu, W. Hu, Q. Guo, *Phys. Rev. E* **2018**, *98*, 022211.
[11] Y. Qiu, B. A. Malomed, D. Mihalache, X. Zhu, L. Zhang, Y. He, *Chaos, Solitons Fractals* **2020**, *131*, 109471.
[12] C. Huang, L. Dong, *Opt. Lett.* **2016**, *41*, 5636.
[13] P. Li, B. A. Malomed, D. Mihalache, *Chaos, Solitons Fractals* **2020**, *137*, 109783.
[14] L. Zeng, Y. Zhu, B. A. Malomed, D. Mihalache, Q. Wang, H. Long, Y. Cai, X. Lu, J. Li, *Chaos, Solitons Fractals* **2022**, *154*, 111586.
[15] H. Sakaguchi, B. A. Malomed, *J. Phys. B: At., Mol. Opt. Phys.* **2022**, *55*, 155301.
[16] L. Zhang, X. Zhang, H. Wu, C. Li, D. Pierangeli, Y. Gao, D. Fan, *Opt. Express* **2019**, *27*, 27936.
[17] C. Tan, T. Lei, M. Zou, Y. Liang, L. Chen, P. Tang, M. Liu, *Opt. Express* **2024**, *32*, 25261.
[18] Y. Zhang, H. Zhong, M. R. Belić, Y. Zhu, W. Zhong, Y. Zhang, D. N. Christodoulides, M. Xiao, *Laser Photonics Rev.* **2016**, *10*, 526.
[19] J. Chen, J. Zeng, *Chaos: An Interdisc. J. Nonlin. Sci.* **2020**, *30*, 6.

© 2025 The Author(s). Laser & Photonics Reviews published by Wiley-VCH GmbH

18638899, 2025, 8, Downloaded from https://onlinelibrary.wiley.com/doi/10.1002/lpor.202401714 by National Research Council, Wiley Online Library on [14/05/2025]. See the Terms and Conditions (https://onlinelibrary.wiley.com/terms-and-conditions) on Wiley Online Library for rules of use; OA articles are governed by the applicable Creative Commons License

[20] Z. Y. Ming Zhong, *Communications Physics* **2023**, *6*, 62.
[21] X. He, Y. Zhai, Q. Cai, R. Li, P. Li, *Chaos, Solitons Fractals* **2024**, *186*, 115258.
[22] P. Li, B. A. Malomed, D. Mihalache, *Opt. Lett.* **2021**, *46*, 3267.
[23] D. V. Strunin, B. A. Malomed, *Phys. Rev. E* **2023**, *107*, 064203.
[24] P. Li, H. Sakaguchi, L. Zeng, X. Zhu, D. Mihalache, B. A. Malomed, *Chaos, Solitons Fractals* **2023**, *173*, 113701.
[25] S. Liu, Y. Zhang, B. A. Malomed, E. Karimi, *Nat. Commun.* **2023**, *14*, 222.
[26] S. Xu, D. H. Reitze, R. Windeler, *Opt. Express* **2004**, *12*, 4731.
[27] A. Monmayrant, S. J. Weber, B. Chatel, *J. Phys. B* **2010**, *43*, 103001.
[28] A. M. Weiner, *Opt. Commun.* **2011**, *284*, 3669.
[29] J. M. Dudley, G. Genty, S. Coen, *Rev. Mod. Phys* **2006**, *78*, 1135.
[30] M. Hary, L. Salmela, P. Ryczkowski, F. Gallazzi, J. M. Dudley, G. Genty, *Opt. Lett.* **2023**, *48*, 4512.
[31] R. Iegorov, T. Teamir, G. Makey, F. Ilday, *Optica* **2016**, *3*, 1312.
[32] W. Ma, Z. Liu, Z. A. Kudyshev, A. Boltasseva, W. Cai, Y. Liu, *Nat. Photonics* **2021**, *15*, 77.
[33] N. N. Akhmediev, A. Ankiewicz, J. M. Soto-Crespo, *Phys. Rev. Lett.* **1997**, *79*, 4047.
[34] G. Herink, F. Kurtz, B. Jalali, D. R. Solli, C. Ropers, *Science* **2017**, *356*, 50.
[35] S. Liu, Y. Cui, E. Karimi, B. A. Malomed, *Optica* **2022**, *9*, 240.
[36] Y. S. Kivshar, G. P. Agrawal, *Optical Solitons: From Fibers to Photonic Crystals*, Academic Press, **2003**.
[37] V. Karpman, *Phys. Rev. E* **1993**, *47*, 2073.
[38] L. F. Mollenauer, R. H. Stolen, J. P. Gordon, *Phys. Rev. Lett.* **1980**, *45*, 1095.
[39] R. H. Stolen, C. Lin, *Phys. Rev. A* **1978**, *17*, 1448.
[40] S. Boscolo, C. Finot, *Shaping Light in Nonlinear Optical Fibers*, John Wiley & Sons, **2017**.
[41] O. Tzang, A. M. Caravaca-Aguirre, K. Wagner, R. Piestun, *Nat. Photonics* **2018**, *12*, 368.
[42] V. Ansari, J. M. Donohue, B. Brecht, C. Silberhorn, *Optica* **2018**, *5*, 534.
[43] H. Zhang, Y. Du, C. Zeng, Z. Sun, Y. Zhang, J. Zhao, D. Mao, *Sci. Adv.* **2024**, *10*, eadl2125.
[44] L. G. Wright, F. O. Wu, D. N. Christodoulides, F. W. Wise, *Nat. Phys.* **2022**, *18*, 1018.
[45] Y. Shen, Q. Zhan, L. G. Wright, D. N. Christodoulides, F. W. Wise, A. E. Willner, K.-h. Zou, Z. Zhao, M. A. Porras, A. Chong, C. Wan, K. Y. Bliokh, C.-T. Liao, C. Hernández-García, M. Murnane, M. Yessenov, A. F. Abouraddy, L. J. Wong, M. Go, S. Kumar, C. Guo, S. Fan, N. Papasimakis, N. I. Zheludev, L. Chen, W. Zhu, A. Agrawal, M. Mounaix, N. K. Fontaine, J. Carpenter, et al., *J. Opt.* **2023**, *25*, 093001.
[46] A. Apolonski, A. Poppe, G. Tempea, C. Spielmann, T. Udem, R. Holzwarth, T. W. Hänsch, F. Krausz, *Phys. Rev. Lett.* **2000**, *85*, 740.
[47] C. Riek, P. Sulzer, M. Seeger, A. S. Moskalenko, G. Burkard, D. V. Seletskiy, A. Leitenstorfer, *Nature* **2017**, *541*, 376.
[48] M. E. Fermann, V. I. Kruglov, B. C. Thomsen, J. M. Dudley, J. D. Harvey, *Phys. Rev. Lett.* **2000**, *84*, 6010.
[49] J. M. Dudley, C. Finot, D. J. Richardson, G. Millot, *Nat. Phys.* **2007**, *3*, 597.
[50] T. Biesenthal, L. J. Maczewsky, Z. Yang, M. Kremer, M. Segev, A. Szameit, M. Heinrich, *Science* **2022**, *376*, 1114.
[51] X. Wu, J. Peng, S. Boscolo, C. Finot, H. Zeng, *Phys. Rev. Lett.* **2023**, *131*, 263802.
[52] B. A. Malomed, in *Fractional Dispersive Models and Applications: Recent Developments and Future Perspectives*, Springer, **2024**, pp. 1–30.
[53] S. Ş. Bayın, *J. Math. Phys.* **2016**, *57*, 123501.
[54] B. Ismail, A. Nakib, F. Heliodore, S. Poullain, P. Siarry, in *2013 IEEE International Symposium on Parallel & Distributed Processing, Workshops and Phd Forum*, IEEE, **2013**, pp. 466–473.
[55] R. Driben, B. A. Malomed, *Opt. Commun.* **2000**, *185*, 439.
[56] A. F. Runge, D. D. Hudson, K. K. Tam, C. M. de Sterke, A. Blanco-Redondo, *Nat. Photonics* **2020**, *14*, 492.
[57] P. Grelu, N. Akhmediev, *Nat. Photonics* **2012**, *6*, 84.
[58] X. Yao, X. Liu, *Photonics Res.* **2018**, *6*, 875.
[59] B. A. Malomed, in *Photonics*, vol. *8*, Mdpi, **2021**, 353.
[60] F. Ilday, J. Buckley, W. Clark, F. Wise, *Phys. Rev. Lett.* **2004**, *92*, 213902.
[61] A. Mahjoubfar, D. V. Churkin, S. Barland, N. Broderick, S. K. Turitsyn, B. Jalali, *Nat. Photonics* **2017**, *11*, 341.
[62] Y. Cui, Y. Zhang, Y. Song, L. Huang, L. Tong, J. Qiu, X. Liu, *Laser Photonics Rev.* **2021**, *15*, 2000216.
[63] A. Monmayrant, B. Chatel, *Rev. Sci. Instrum.* **2004**, *75*, 2668.
[64] M. Tan, X. Xu, A. Boes, B. Corcoran, T. G. Nguyen, S. T. Chu, B. E. Little, R. Morandotti, J. Wu, A. Mitchell, D. J. Moss, *arXiv preprint arXiv:2401.07197* **2024**.
[65] V. T. Hoang, J. Widjaja, Y. Qiang, M. Liu, T. J. Alexander, A. F. Runge, C. M. de Sterke, *arXiv preprint arXiv:2410.23671* **2024**.
[66] Z. Wang, M. He, X. Ling, L. Zhang, C. Zhao, *Opt. Lett.* **2024**, *49*, 5499.
[67] L. G. Wright, D. N. Christodoulides, F. W. Wise, *Science* **2017**, *358*, 94.
[68] D. Hui, H. Alqattan, S. Zhang, V. Pervak, E. Chowdhury, M. T. Hassan, *Sci. Adv.* **2023**, *9*, eadf1015.
[69] N. Laskin, *Phys. Rev. E* **2000**, *62*, 3135.
[70] A. Vithya, M. Mani Rajan, S. Arun Prakash, *Nonlinear Dyn.* **2018**, *91*, 687.
[71] A. Zheltikov, *Opt. Commun.* **2023**, 129766.

© 2025 The Author(s). Laser & Photonics Reviews published by Wiley-VCH GmbH

18638899, 2025, 8, Downloaded from https://onlinelibrary.wiley.com/doi/10.1002/lpor.202401714 by National Research Council, Wiley Online Library on [14/05/2025]. See the Terms and Conditions (https://onlinelibrary.wiley.com/terms-and-conditions) on Wiley Online Library for rules of use; OA articles are governed by the applicable Creative Commons License